Planetary and Space Science 131 (2016) 60–69

Contents lists available at ScienceDirect

Planetary and Space Science

journal homepage: www.elsevier.com/locate/pss

Comparing wind directions inferred from Martian dust devil tracks analysis with those predicted by the Mars Climate Database

T. Statella [a,*], P. Pina [b], E.A. Silva [c], Ary Vinicius Nervis Frigeri [a], Frederico Gallon Neto [a]

[a] Instituto Federal de Educação, Ciência e Tecnologia de Mato Grosso – IFMT, 95 Zulmira Canavarro780025-200, Cuiabá, Brazil
[b] CERENA, Instituto Superior Técnico - IST, Universidade de Lisboa, Av. Rovisco Pais1049-001, Lisboa, Portugal
[c] Universidade Estadual Paulista, Faculdade de Ciências e Tecnologia – FCT, 305 Roberto Simonsen19060-900, Presidente Prudente, Brazil

ARTICLE INFO

Article history:
Received 7 December 2015
Received in revised form
7 June 2016
Accepted 21 July 2016
Available online 25 July 2016

ABSTRACT

We have calculated the prevailing dust devil tracks direction as a means of verifying the Mars Climate Database (MCD) predicted wind directions accuracy. For that purpose we have applied an automatic method based on morphological openings for inferring the prevailing tracks direction in a dataset comprising 200 Mars Orbiter Camera (MOC) Narrow Angle (NA) and High Resolution Imaging Science Experiment (HiRISE) images of the Martian surface, depicting regions in the Aeolis, Eridania, Noachis, Argyre and Hellas quadrangles. The prevailing local wind directions were calculated from the MCD predicted speeds for the WE and SN wind components. The results showed that the MCD may not be able to predict accurately the locally dominant wind direction near the surface. In adittion, we confirm that the surface wind stress alone cannot produce dust lifting in the studied sites, since it never exceeds the threshold value of 0.0225 Nm^{-2} in the MCD.

1. Introduction

Dust devils are small whirlwinds made visible by entrained dust and sand. They are upward moving, spiraling flows caused by heating of near-surface air by insolation (Balme and Greeley, 2006). Dust devils activity is easily identified in remotely sensed images by the tracks they often leave behind. Dust devil tracks are albedo patterns on planetary surfaces that result from the removal of particles by the presence of a dust devil to expose an underlying surface with a different albedo. On Mars, dust devil tracks densities were shown to change with the time of the year, suggesting that dust devil activity also depends on the season of the year (Thomas et al., 2003; Whelley and Greeley, 2006). Those albedo features tend to fade with time, which is attributed to the deposition of dust (Malin and Edgett, 2001; Balme et al., 2003). In a period of a few months (2 to 4 months) old tracks can be recovered by dust and replaced by new tracks (Statella et al., 2015).

Important information that can be obtained by the analysis of the tracks is the trajectory of the vortices, which can be used to infer the prevailing wind orientation near the surface, as dust devils are typically thought to move, on average, in the direction of the dominant wind (Rennó et al., 1998). The inference of the wind direction based on aeolian features is one of the few procedures for verifying circulation models of the Martian atmosphere. As a plethora of orbital images of the surface of Mars has been made available, automatic methods can be developed and applied to detect (Statella et al., 2012) and measure the orientation of dust devil tracks.

The prevailing direction of the wind at specific locations on the surface of Mars for a certain solar longitude can be estimated from extractions of the Mars Climate Database (MCD). Such extractions can then be compared to the prevailing direction of dust devil tracks previously detected (Statella et al., 2012) in Mars Orbiter Camera (MOC) Narrow Angle (NA) and High Resolution Imaging Science Experiment (HiRISE) images at the same locations. From the detected dust devil tracks we could estimate the prevailing track direction for each image by using the Directional Morphological Openings by Linear Structuring Elements, as proposed by Statella et al. (2014). The prevailing direction of dust devil tracks for each scene has been compared to the MCD extractions in order to find out if the MCD information could be used to describe local wind patterns on the surface of Mars.

2. Image Dataset

The image dataset from which we have detected the dust devil tracks was made up of 124 images: 75 MOC narrow angle panchromatic band and 49 HiRISE red band from Aeolis, Argyre,

* Corresponding author.
E-mail addresses: thiago.statella@cba.ifmt.edu.br (T. Statella), ppina@tecnico.ulisboa.pt (P. Pina), erivaldo@fct.unesp.br (E.A. Silva), aryviniciusnf@gmail.com (A.V. Nervis Frigeri), fredgneto@gmail.com (F.G. Neto).

http://dx.doi.org/10.1016/j.pss.2016.07.004
0032-0633/

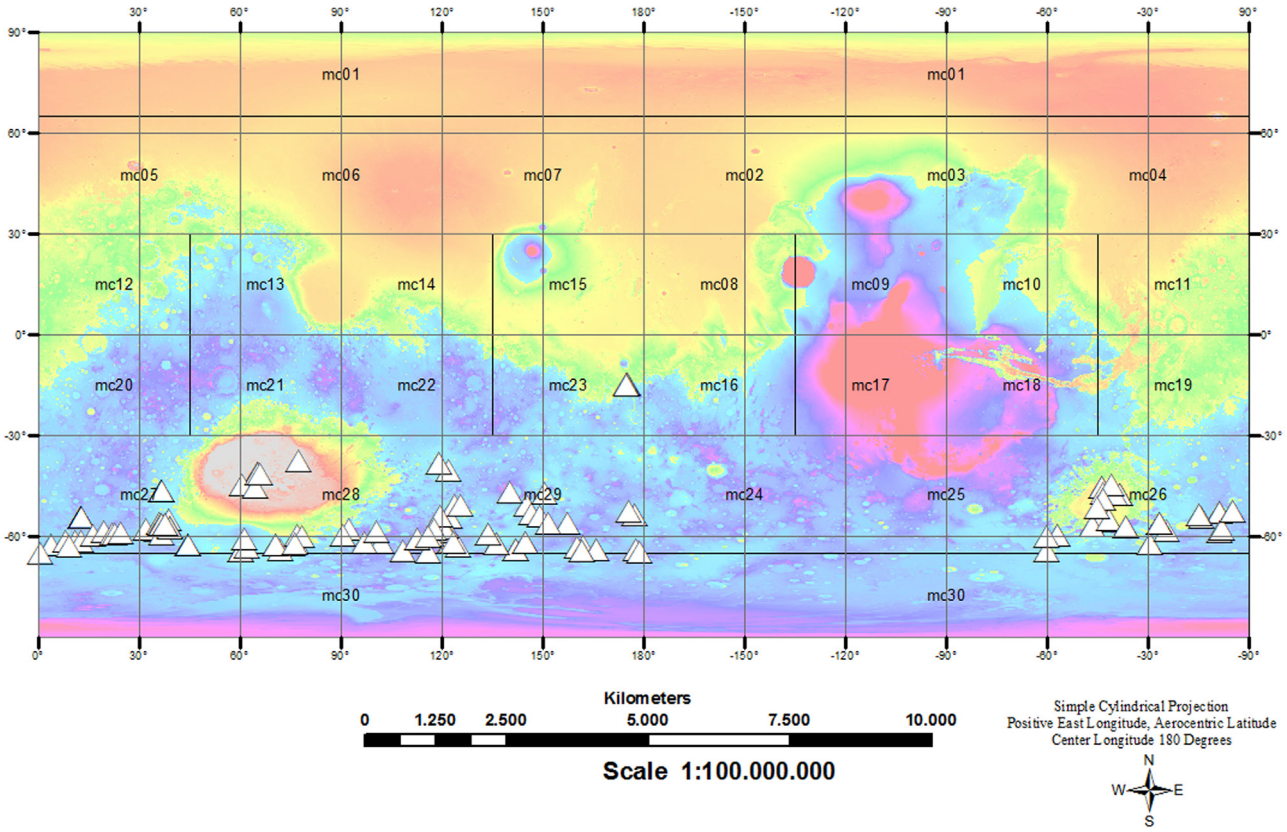

Fig. 1. Distribution of the image dataset: Aeolis (MC23), Argyre (MC26), Noachis (MC27), Hellas (MC28) and Eridania (MC29). The white triangles represent the center coordinates of the original scenes. Image credits: R.K. Hayward, K.F. Mullins, L.K. Fenton, T.M. Hare, T.N. Titus, M.C. Bourke, A. Colaprete, P.R. Christensen.

Noachis, Hellas and Eridania quadrangles defined by Mars Charts (MC, as defined by the USGS mapping quadrangles) 23, 26, 27, 28 and 29, respectively. By having detected the dust devil tracks we mean that the image dataset was formed by a set of binary images in which pixels belonging to tracks have been labeled with value 1 (white) and pixels not belonging to tracks have been labeled with value 0 (black). The detection procedure has been fully described in Statella et al. (2012). The spatial resolution of HiRISE images was either 0.25 m (~90% of the images) or 0.50 m while the MOC spatial resolution varied from 1.43 m to 8.75 m (mean ~5 m). Some of them were cropped into several regions of interest, enlarging the image dataset to 200 images (90 MOC and 110 HiRISE). Fig. 1 shows the distribution of the initial set (before cropping procedure) of 124 images (white triangles) according to their center coordinates in the planetocentric coordinate system. The base map is the Mars Orbiter Laser Altimeter (MOLA) topography layer of the Mars Global Digital Dune Database. In order to infer the prevailing wind direction from dust devil tracks we have used one of the methods proposed by Statella et al. (2014), namely, the Directional Morphological Openings by Linear Structuring Elements method. The input for this method is a binary image showing detected dust devil tracks in white and the background in black. Dust devil tracks had been previously detected in the 200 images using the method proposed by Statella et. al (2012), with a global accuracy of 92% $\pm$ 5%.

3. Inferring the prevailing wind direction from dust devil tracks

Dust devils are typically thought to move, on average, in the direction of the prevailing surface wind (Rennó et al.,1998). The prevailing wind direction can then be inferred by calculating the prevailing dust devil tracks direction in orbital images. For that purpose we have adopted one of the methods developed by Statella et al. (2014), namely, the Directional Morphological Openings by Linear Structuring Elements. This method is based on Mathematical Morphology (MM), a theory developed by Georges Matheron and Jean Serra in the 1960s, which is highly adequate to deal with the geometric features of structures. A few definitions of the theory, useful to fully explain the Directional Morphological Openings by Linear Structuring Elements method, are given below.

Let us first define a digital image as follows: Let E be a nonempty set of adjacent squares arranged in rows and columns, forming a rectangular surface. Let K be a set of gray levels. A gray level image is a mapping $E \rightarrow K$. Usually, K belongs to the interval $[0, K]$ in Z with $E \in Z^2$.

Then we can define the major mathematical morphology transformations, Erosion and Dilation:

Let B be a subset from Z^2, $B \subset E$. The Erosion (Soille, 2004), ε, of an image f by B is the minimum of the translation of f by the vectors $-b$ of B. B is called Structuring Element (SE).

$$\varepsilon_B(f) = \bigwedge_{b \in B} f_{-b} \quad (1)$$

The Dilation (Soille, 2004), δ, of f by a SE B is the maximum of the translation of f by the vectors b of B.

$$\delta_B(f) = \bigvee_{b \in B} f_b \quad (2)$$

The structuring element B is a completely defined and known (size and shape) set which is compared, in a transformation, to the image unknown set. The result of this transformation allows us to evaluate the unknown set. Based on Erosion and Dilation transformations we can define the morphological Opening. The Opening, γ, of f by a structuring element B is the erosion of f by B followed by a dilation by B transposed (Soille, 2004):

$$\gamma_B(f) = \delta_{B*}\left[\varepsilon_B(f)\right]. \quad (3)$$

A morphological Opening will remove from the image all the regions of the image whose shape and size do not fully contain the structuring element. Linear Structurig Elements (LSEs) can be arranged in several orientations so that a morphological Opening can provide information about the directions of binary sets in an digital image. Let us now define a set of directions $\alpha \in Z^+$, measured clockwise from North in steps of n degrees. For $n = 15°$, we then have the set of directions $\alpha = \{0°, 15°,.., 345°\}$. The direction opposed to α is denoted α', so if $\alpha = 0°$ then $\alpha' = 180°$. The path in the direction α is defined as the union of the radii of the LSE in the directions d and d'. As an example, the path in the direction 45° is composed by the radii (with origin in a given pixel p) oriented to 45° and 225° (one can notice that the path in the direction 225° is identical to the path in the direction 45°, as both paths share the same radii). Now it is possible to define a family $L_{\alpha,\lambda}$ (with direction α and size λ) of line SEs whose paths are oriented in the directions $\alpha = \{0°, 15°,.., 165°\}$. As examples, LSEs with sizes $\lambda=1$ in the directions 0°, 45°, 90° and 135° are:

$$B_0 = \begin{bmatrix} 0 & 1 & 0 \\ 0 & 1 & 0 \\ 0 & 1 & 0 \end{bmatrix}, B_{45} = \begin{bmatrix} 0 & 0 & 1 \\ 0 & 1 & 0 \\ 1 & 0 & 0 \end{bmatrix},$$

$$B_{90} = \begin{bmatrix} 0 & 0 & 0 \\ 1 & 1 & 1 \\ 0 & 0 & 0 \end{bmatrix}, B_{135} = \begin{bmatrix} 1 & 0 & 0 \\ 0 & 1 & 0 \\ 0 & 0 & 1 \end{bmatrix}$$

The choice for the angular steps of 15° derives from the digital approximations performed when building linear structuring elements in a square digital grid, that is, increasing the number of angular steps after this level of detail would not provide much more meaningful information.

The main advantage of this method is the high capability of directional Openings to estimate the prevailing orientation of dust devil tracks as Mathematical Morphology operators are crafted on the analysis of the geometry and topology of object features.

After applying Openings with LSEs of size λ in the directions $\alpha = \{0°, 15°,.., 165°\}$, the prevailing direction of the tracks is assumed to be the one in which the Opening has removed less pixels than in any other directions, that is, the direction where the structuring element better fits the tracks. The size λ of the LSEs varied from scene to scene (but, for each image, the size was fixed) according to the maximum width of the tracks in each scene. The width of the tracks in each scene is calculated as described in Statella et al. (2016). When plotting the results in a direction diagram, where each wing of the diagram represents the amount of pixels removed by the Opening, one should look for the smallest wing to determine

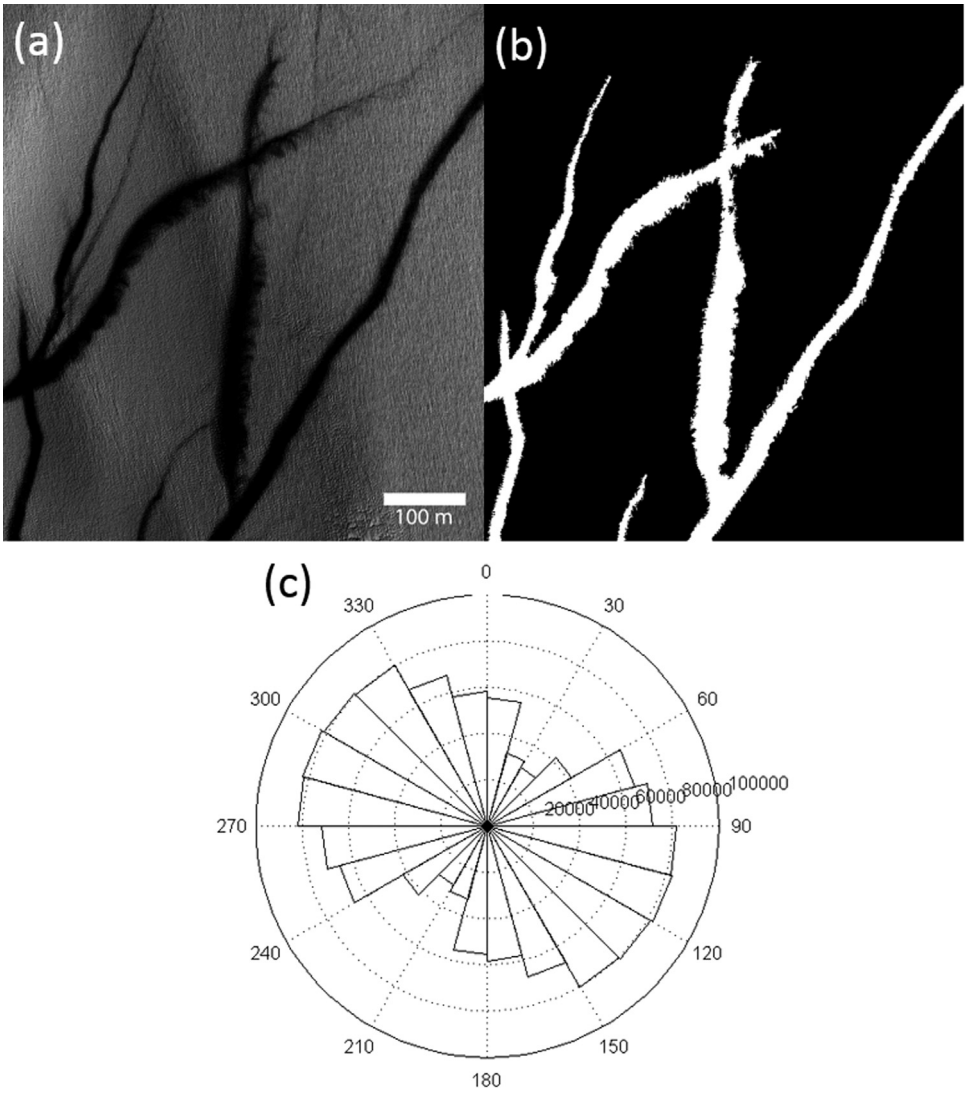

Fig. 2. Region of interest in HiRISE image PSP_006163_1345 (a); Automated tracks detection (b); (c) Diagram of directions (note that the less frequented classes are the ones less modified by the LSE and thus the ones corresponding to the prevailing orientions). [Original image credits: NASA/JPL/University of Arizona].

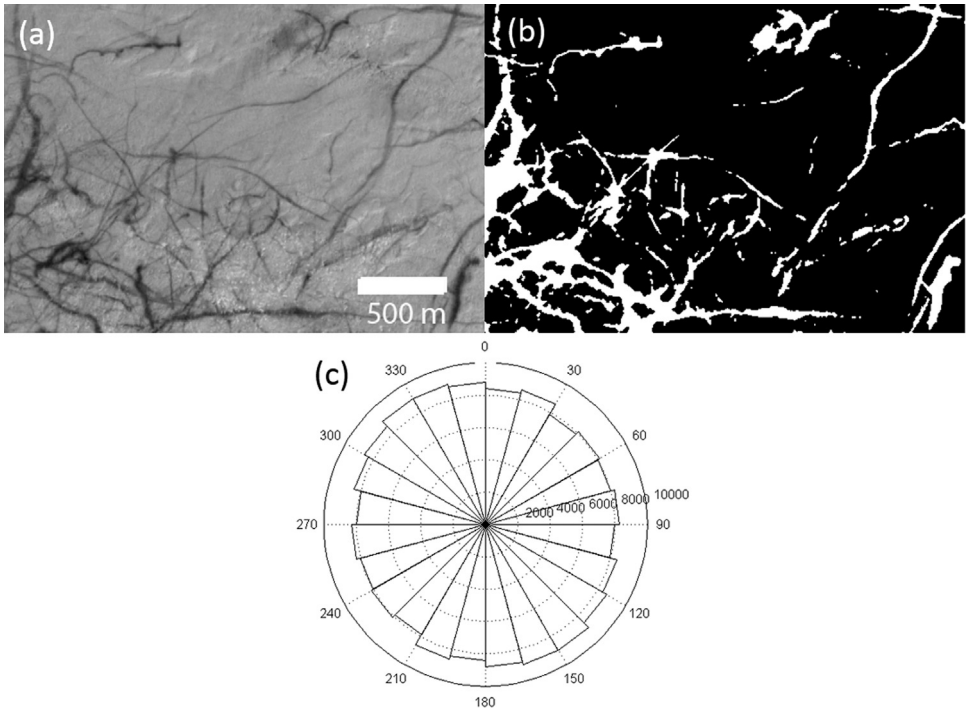

Fig. 3. Region of interest in MOC NA image E13-00271 (a); Automated tracks detection (b); (c) Diagram of directions (note that the less frequented classes are the ones less modified by the LSE and thus the ones corresponding to the prevailing orientions). [Original image credits: NASA/JPL/MSSS].

the prevailing direction. Consider, as an example, a region of interest of the image HiRISE PSP_006163_1345 from Argyre quadrangle shown in Fig. 2a. The binary image shown in Fig. 2b is the result of the dust devil tracks detection, which has been used as input for estimating the prevailing direction of the winds in that scene. In Fig. 2c we show the direction diagram for that image. The prevailing wind direction inferred from this image by the presented method is the less frequented one, that is, 30°–210°.

Fig. 3 shows another example, this time for the MOC NA image E13-00271, also from Argyre quadrangle. As we can observe in Fig. 3a, tracks do not seem to follow any preferential direction as they do in HiRISE image PSP_006163_1345. Thus, we cannot infer, visually, any preferable direction. Nevertheless, after applying the directional morphological openings we could estimate the prevailing direction as being ~30°–210°.

4. Results

Morphological Openings with LSEs oriented in the directions $\alpha = \{0°, 15°,., 165°\}$ have been applied to the image dataset in order to automatically infer the prevailing dust devil tracks direction. The size λ of the LSEs varied from scene to scene (but, for each image, the size was fixed) according to the maximum width of the tracks in each scene (this procedure has been adopted in order to avoid a possible influence of the width of the tracks in the results). Tracks width had been calculated as described in Statella et al. (2016). We show the results per region and per solar longitude L_s (in angular intervals of 30°) in the Tables 1–5, where it can be seen the varation in dust devil tracks directon with the season of the year. The solar longitude is the Mars-Sun angle, measured from the Northern Hemisphere spring equinox where $L_s = 0°$. Intervals of 30° in solar longitude represent the passage of a martian month. Therefore, for the Northern Hemisphere we have: from $L_s = 0°$ to 90° the spring season (autumn for the Southern Hemisphere), from $L_s = 90°$ to 180° the summer season (winter for the Southern Hemisphere), from $L_s = 180°$ to 270° the autumn season (spring for the Southern Hemisphere) and from $L_s = 270°$ to 360° the winter season (summer for the Southern Hemisphere). The prevailing direction for a given interval in solar longitude, for example 0°-30°, has been adopted as being the modal value among all directions measured in all scenes whose solar longitudes fall in that interval.

Table 1
Prevailing dust devil tracks directions for Aeolis quadrangle.

Solar LongitudeL_s[deg.]	Season	N° of images	Prevailing direction [deg.]
0-30	Autumn	1	120-300
120-150	Winter	1	105-285
240-270	Spring	2	105-285/45-225
330-360	Summer	1	120-300

Table 2
Prevailing dust devil tracks directions for Argyre quadrangle.

Solar LongitudeL_s[deg.]	Season	N° of images	Prevailing direction [deg.]
240-270	Spring	7	45-225
270-300	Summer	7	0-180
300-330	Summer	15	30-210
330-360	Summer	42	45-225

Table 3
Prevailing dust devil tracks directions for Noachis quadrangle.

Solar LongitudeL_s[deg.]	Season	N° of images	Prevailing direction [deg.]
180-210	Spring	3	120-300/0-180/60-240
210-240	Spring	1	90-270
240-270	Spring	7	165-345
270-300	Summer	15	165-345
330-360	Summer	13	15-195

Table 4
Prevailing dust devil tracks directions for Hellas quadrangle.

Solar LongitudeL_s[deg.]	Season	N° of images	Prevailing direction [deg.]
240-270	Spring	3	165-345/90-270/135-193
270-300	Summer	11	90-270
300-330	Summer	25	30-210
330-360	Summer	1	135-315

Table 5
Prevailing dust devil tracks directions for Eridania quadrangle.

Solar LongitudeL_s[deg.]	Season	N° of images	Prevailing direction [deg.]
240-270	Spring	14	120-300
270-300	Summer	18	0-180
300-330	Summer	11	75-255/90-270/105-285
330-360	Summer	2	0-180

In Table 1 we can see that the prevailing tracks directions follow a pattern SE-NW for solar longitudes intervals 0°–30° (autumn), 120°–270° (winter/spring) and 120°–300° (winter/spring/summer). For solar longitudes ranging from 240° to 270° (spring) we found two dominant directions, which are 105°–285° and 45°–225°. The large difference between those two directions is believed to have been caused by the fact that we had only two images from Aeolis quadrangle.

For Argyre quadrangle, whose results are shown in Table 2, we have found a pattern NE-SW for the orientation of the tracks. For Noachis quadrangle, as shown in Table 3, we have found different results for the prevailing tracks directions among the solar longitude intervals. For solar longitudes ranging from 240° to 270° (spring) and from 270° to 300° (summer) a pattern SE-NW can be seen. From 180° to 210° (spring) the dominant tracks directions do not show a preferable direction and from 210° to 240° (spring), tracks directions inferred from the one image in that interval followed the E-W orientation.

In Table 4, the prevailing dust devil tracks directions calculated for Hellas quadrangle were 90°–270° (E-W) for images acquired during the solar longitudes from 270° to 300° (summer), 30°–310° for images whose solar longitudes fall in the interval 300° to 330° (summer) and 135°–315° for the one image whose solar longitude falls in the interval 330° to 360°(summer). For the 240°–270° (spring) solar longitude interval the images showed no unique modal value. Instead, the tracks are mainly oriented in three directions.

In Table 5 we show the results for Eridania quadrangle. For solar longitudes ranging from 270° to 300° (summer) and from 330° to 360° (summer) the tracks follow a E-W pattern. The prevailing directon changes for 120°–300° for images in the interval 240°–270° (spring) and we found three modal values for images with solar longitudes ranging from 300° to 330° (summer).

In Tables 6–10 we show the directions calculated for each image of the quadrangles Aeolis, Argyre, Noachis, Hellas and Eridania, the CPBL height, the solar longitude and the local time acquisition for each image and the directions of the winds predicted by the MCD. The MCD is a database of atmospheric statistics compiled from the Global Climate Model (GCM) and respective numerical simulations of the Martian atmosphere (Forget et al., 1999; Lewis et al., 1999). It was developed by the Laboratoire de Météorologie Dynamique (LMD, Paris), Atmospheric, Oceanic and Planetary Physics group (AOPP, Oxford), Department of Physics and Astronomy (The Open University) and Instituto de Astrofísica de Andalucía (IAA, Granada) with the support of the European Space Agency and the Centre National d'Etudes Spatiales and the outputs provided by the MCD are based on large-scale climatological means.

The extractions have been done according to the solar longitude, acquisition date and time, latitude and longitude of each scene, at three different altitudes from surface: 50 m, 1000 m and at the Convective Planetary Boundary Layer (CPBL) height. The Martian Planetary Boundary Layer (PBL) is the portion of the atmosphere closest to the surface, within which interactions between the atmosphere and the surface itself are active. In practice, this represents the lowest portion of the atmosphere, within which surface-driven intense convection may take place, forming convective plumes and vortices during the day (Haberle et al., 1993; Hinson et al., 2008; Petrosyan et al., 2011).

The height of the PBL and, in particular, the height of daytime CPBL, is a key quantity describing the vigor of convective activity, that changes over the surface according to the local thickness of the atmosphere layer. Examples of estimated PBL heights inferred from lander measurements, from heights of convective clouds, from temperature profiles or radio occultation are given by Fenton and Lorenz (2015) and a more extensive study is given by Hinson et al. (2008).

We have chosen the altitudes in our extractions from the MCD so that they match the lower CPBL, which is 1000 m from the surface, and the upper CPBL limit, which has been obtained from the MCD for each image center coordinates. Fenton and Lorenz (2015) have performed a study on Amazonis Planitia and have found out that the CPBL thickness can be estimated as being ~5 times the median of the active dust devil plumes, after analyzing MRO CTX images. As we are rather working with dust devil tracks instead of plumes, we cannot infer such relationship and, therefore, we have decided to consider the upper limit of the CPBL in the experments. In addition, we have run the predictions at 50 m from the surface in order to see if the wind directions could differ significantly from those in the CPBL and if the portion of the atmosphere closer to the surface could play a more dominant role in the directions of the dust devils. For the experiments we have used the MCD version 5.2 and we have adopted the climatology average solar dust scenario for it is the most representative of a standard condition. Running the extractions with Mars Years (MY) scenarios corresponding to the acquisition date of the images in a sample of the dataset did not show significant (i. e., were not larger than the 15° of the precision of the method used to calculate directions in the images) differences when compared with the climatology

Table 6
Comparison between calculated prevailing wind direction and predicted wind direction for Aeolis.

ID	L_s[deg.]	Local Time	Calculated [deg.]	CPBL [m]	Predicted [deg.]		
					50 m	1000 m	CPBL
E16-01962	18.77	13:39	120-300	4500	45-225	45-225	30-210
R02-00357	134.17	14:40	105-285	5500	30-210	15-195	0-180
PSP_003834_1650	242.6	15:14	120-300	6300	90-270	90-270	75-255
R08-02402	249.25	14:27	105-285	6300	105-285	90-270	90-270
R13-01467	331.03	13:31	120-300	5600	60-240	60-240	45-225

Table 7
Comparison between calculated prevailing wind direction and predicted wind direction for Argyre.

ID	L_s[deg.]	Local Time	Calculated [deg.]	CPBL [m]	Predicted [deg.]		
					50 m	1000 m	CPBL
M10-01206	260.85	14:09	165-345	4800	120-300	120-300	0-180
S08-02952	257.68	14:24	90-270	6400	30-210	15-195	30-210
R08-02621_P1	250.90	14:40	0-180	6300	45-225	30-210	30-210
R08-02621_P2	250.90	14:40	120-300	6300	45-225	30-210	30-210
S08-03151	259.03	14:18	45-225	5000	0-180	0-180	0-180
ESP_012927_1245	256.30	15:24	60-240	4500	75-255	75-255	60-240
ESP_013204_1260	270.00	15:11	45-225	4600	90-270	75-255	75-255
S10-01582	297.27	13:52	75-255	6200	165-345	165-345	0-180
S10-01598	297.32	13:46	15-195	4600	30-210	30-210	30-210
ESP_013310_1200_P1	275.10	15:07	165-345	6200	0-180	0-180	165-345
ESP_013310_1200_P2	275.10	15:07	75-255	6200	0-180	0-180	165-345
ESP_013626_1245	290.40	15:02	120-300	4700	120-300	105-285	105-345
ESP_013520_1180_P1	285.30	14:58	120-300	6400	120-300	120-300	165-345
ESP_013520_1180_P2	285.30	14:58	105-285	6400	120-300	120-300	165-345
E13-00271_P1	320.78	13:28	30-210	5600	120-300	120-300	150-330
E13-00271 _P2	320.78	13:28	75-255	5600	120-300	120-300	150-330
M14-00175_P1	329.22	13:22	0-180	4200	30-210	30-210	75-255
M14-00175_P2	329.22	13:22	105-285	4200	30-210	30-210	75-255
M12-02214	305.76	13:30	15-198	4300	60-240	60-240	60-240
ESP_013996_1155	307.60	14:42	30-210	5700	90-270	90-270	135-315
ESP_014049_1200	310.10	14:38	45-225	5700	45-225	45-225	15-195
ESP_014259_1230_P1	319.50	14:32	0-180	4600	135-315	120-300	90-270
ESP_014259_1230_P2	319.50	14:32	30-210	4600	135-315	120-300	90-270
PSP_005596_1245	326.20	14:28	90-270	4200	90-270	90-270	90-270
PSP_005397_1270_P1	317.40	14:29	60-240	6000	105-285	105-285	135-315
PSP_005397_1270_P2	317.40	14:29	105-285	6000	105-285	105-285	135-315
PSP_005397_1270_P3	317.40	14:29	75-255	6000	105-285	105-285	135-315
PSP_005397_1270_P4	317.40	14:29	75-255	6000	105-285	105-285	135-315
PSP_005397_1270_P5	317.40	14:29	90-270	6000	105-285	105-285	135-315
E14-00400_P1	339.47	13:26	0-180	4100	30-210	30-210	75-255
E14-00400_P2	339.47	13:26	135-315	4100	30-210	30-210	75-255
E14-00400_P3	339.47	13:26	0-180	4100	30-210	30-210	75-255
R13-02691	334.68	13:45	0-180	5300	105-285	105-285	120-300
PSP_005820_1320_P1	335.70	14:25	30-210	4200	30-210	30-210	60-240
PSP_005820_1320_P2	335.70	14:25	45-225	4200	30-210	30-210	60-240
PSP_005820_1320_P3	335.70	14:25	45-225	4200	30-210	30-210	60-240
PSP_005820_1320_P4	335.70	14:25	45-225	4200	30-210	30-210	60-240
PSP_005820_1320_P5	335.70	14:25	45-225	4200	30-210	30-210	60-240
PSP_005820_1320_P6	335.70	14:25	30-210	4200	30-210	30-210	60-240
PSP_005820_1320_P7	335.70	14:25	165-345	4200	30-210	30-210	60-240
PSP_005820_1320_P8	335.70	14:25	45-225	4200	30-210	30-210	60-240
PSP_005846_1235_P1	336.80	14:29	75-255	5400	105-285	105-285	150-330
PSP_005846_1235_P2	336.80	14:29	75-255	5400	105-285	105-285	150-330
PSP_005846_1235_P3	336.80	14:29	105-285	5400	105-285	105-285	150-330
PSP_005846_1235_P4	336.80	14:29	105-285	5400	105-285	105-285	150-330
PSP_005846_1235_P5	336.80	14:29	90-270	5400	105-285	105-285	150-330
PSP_005846_1235_P6	336.80	14:29	105-285	5400	105-285	105-285	150-330
PSP_005846_1235_P7	336.80	14:29	105-285	5400	105-285	105-285	150-330
PSP_005846_1235_P8	336.80	14:29	0-180	5400	105-285	105-285	150-330
PSP_005846_1235_P9	336.80	14:29	45-225	5400	105-285	105-285	150-330
PSP_005846_1235_P10	336.80	14:29	105-285	5400	105-285	105-285	150-330
PSP_005846_1235_P11	336.80	14:29	75-255	5400	105-285	105-285	150-330
PSP_005846_1235_P12	336.80	14:29	60-240	5400	105-285	105-285	150-330
PSP_005846_1235_P13	336.80	14:29	90-270	5400	105-285	105-285	150-330
PSP_005846_1235_P14	336.80	14:29	120-300	5400	105-285	105-285	150-330
PSP_005846_1235_P15	336.80	14:29	165-345	5400	105-285	105-285	150-330
PSP_005846_1235_P16	336.80	14:29	30-210	5400	105-285	105-285	150-330
PSP_005846_1235_P17	336.80	14:29	120-300	5400	105-285	105-285	150-330
PSP_005846_1235_P18	336.80	14:29	45-225	5400	105-285	105-285	150-330
PSP_005846_1235_P19	336.80	14:29	60-240	5400	105-285	105-285	150-330
PSP_005846_1235_P20	336.80	14:29	15-195	5400	105-285	105-285	150-330
PSP_005846_1235_P21	336.80	14:29	90-270	5400	105-285	105-285	150-330
PSP_005846_1235_P22	336.80	14:29	15-195	5400	105-285	105-285	150-330
PSP_006163_1345_P1	349.80	14:28	30-210	4200	0-180	0-180	15-195
PSP_006163_1345_P2	349.80	14:28	30-210	4200	0-180	0-180	15-195
PSP_006163_1345_P3	349.80	14:28	45-225	4200	0-180	0-180	15-195
PSP_006163_1345_P4	349.80	14:28	60-240	4200	0-180	0-180	15-195
PSP_006176_1225_P1	350.40	14:34	135-315	4200	105-285	105-285	90-270
PSP_006176_1225_P2	350.40	14:34	120-300	4200	105-285	105-285	90-270
PSP_006176_1225_P3	350.40	14:34	150-330	4200	105-285	105-285	90-270
PSP_005780_1215	334.00	14:30	105-285	5500	105-285	105-285	105-285

Table 8
Comparison between calculated prevailing wind direction and predicted wind direction for Noachis.

ID	L_s[deg.]	Local Time	Calculated [deg.]	CPBL [m]	Predicted [deg.]		
					50 m	1000 m	CPBL
PSP_002548_1255_P1	181.80	16:00	120-300	2600	60-240	75-255	75-255
PSP_002548_1255_P2	181.80	16:00	60-240	2600	60-240	75-255	75-255
PSP_002548_1255_P3	181.80	16:00	120-300	2600	60-240	75-255	75-255
PSP_003326_1255	217.80	15:53	75-255	4900	75-255	75-255	105-285
PSP_004038_1255	257.70	15:20	75-255	6300	135-315	135-315	75-255
PSP_004249_1255	263.10	15:11	15-195	6600	135-315	135-315	60-240
R0903467	267.72	14:22	135-315	6100	165-345	165-345	150-330
S09-01660_P1	269.93	14:12	165-345	6200	165-345	165-345	150-330
S09-01660_P2	269.93	14:12	165-345	6200	165-345	165-345	150-330
S09-00929_P1	265.39	14:17	0-180	6100	165-345	165-345	150-330
S09-00929_P2	265.39	14:17	165-345	6100	165-345	165-345	150-330
ESP_013321_1175	275.70	15:08	135-315	6000	150-330	150-330	120-300
ESP_013557_1245	287.10	14:52	165-345	6400	165-345	165-345	135-315
E11-01722	287.99	13:52	30-210	5900	165-345	165-345	0-180
E11-03103	293.62	13:48	0-180	5700	165-345	165-345	0-180
E11-00747	284.82	13:55	30-210	6100	150-330	150-330	0-180
E11-01129	286.08	13:53	90-270	6400	150-330	150-330	0-180
E11-01527	287.34	13:51	60-240	6400	150-330	150-330	165-345
E11-03844	297.33	13:43	30-210	5900	150-330	150-330	165-345
E11-02963	292.98	13:46	15-195	6100	150-330	150-330	165-345
E11-00582	284.17	13:54	45-225	6400	150-330	150-330	165-345
E11-01314	286.68	13:51	0-180	6300	165-345	165-345	165-345
R10-04224	285.72	14:08	165-345	6100	150-330	150-330	165-345
R10-02844	281.23	14:08	165-345	6300	165-345	165-345	150-330
R10-04196	285.67	14:03	30-210	6400	165-345	165-345	150-330
R10-00382	272.25	14:17	150-330	6200	165-345	165-345	150-330
R11-03714	304.30	13:50	15-195	5500	165-345	150-330	135-315
PSP_005238_1255	310.30	14:33	120-300	6400	120-300	135-315	150-330
PSP_005383_1255	316.80	14:26	0-180	6100	120-300	120-300	150-330
PSP_005528_1255	323.20	14:20	105-285	5900	105-285	120-300	135-315
ESP_013992_1170_P1	307.50	14:41	0-180	5600	150-330	150-330	150-330
ESP_013992_1170_P2	307.50	14:41	15-195	5600	150-330	150-330	150-330
ESP_013992_1170_P3	307.50	14:41	30-210	5600	150-330	150-330	150-330
ESP_014020_1150	308.70	14:42	30-210	5300	165-345	165-345	165-345
ESP_014322_1215	322.30	14:38	15-195	5300	135-315	135-315	120-300
PSP_005659_1335_P1	328.90	14:24	15-195	6000	75-255	75-255	90-270
PSP_005659_1335_P2	328.90	14:24	0-180	6000	75-255	75-255	90-270
PSP_005659_1335_P3	328.90	14:24	0-180	6000	75-255	75-255	90-270
E12-01041	306.48	13:38	150-330	5400	165-345	165-345	150-330

average solar dust scenario. As the MYs scenarios are produced from irregularly observations, which are subsequently gridded into a regular network by kriging, and as we had no means to assess and compare the accuracy of the MYs scenarios against the average solar dust scenario, we have run the experiments with this last scenario. Regarding the time used for the extractions, we have chosen it to match each image acquisition time. As we cannot know the exact time of dust devil formation, some approximated time value should be adopted. In general, the image acquisition time is very close the peak time of the formation of the convective plumes, therefore, we have adopted that time for the extractions from the MCD. Experiments carried out on a subsample set of images showed that extractions from an interval of ± 1 hour centered at the time of acquisition did not result in differences larger than the precision of the method used for calculating the wind direction from the tracks.

Information about winds from the MCD is based on large-scale (computed for regions of a few degrees in latitude and longitude) climatological means, therefore, the locally prevailing winds that drive the dust devil can be expected to be influenced by regional and local conditions which may not be resolved at the grid scale of the MCD.

In the extractions, the MCD provides wind speeds defined by two components: the meridional SN wind (positive when oriented from south to north) and the zonal WE wind (positive when oriented from west to east) in m/s. The resulting wind direction has been defined as:

$$\alpha = \tan^{-1}(WE/SN) \quad (4)$$

for $WE > 0$ and $SN > 0$. If $WE > 0$ and $SN < 0$, then $\alpha = 180° - |\alpha|$; if $WE < 0$ and $SN < 0$, then $\alpha = 180° + |\alpha|$; and if $WE < 0$ and $SN > 0$, then $\alpha = 360° - |\alpha|$.

Albeit MOC NA and HiRISE images are projected in Sinusoidal and Equirectangular systems, respectively, which are not conformal projections, the errors involved in estimating directions from that remotely sensed data can be considered negletable in the present case. Statella (2015) showed that the maximum angular distortion for a typical HiRISE image is ~0.6°. And for a typical MOC NA image it is ~0.02°, even though meridians are not straight lines in the Sinusoidal projection.

For the comparison between the wind directions inferred from dust devil tracks and the predicted wind directions from the MCD we have considered a tolerance of 15° (which was the angular step used in the directions measurements) for the differences obtained. Therefore, when the difference between the calculated dust devil track prevailing direction and the MCD predicted wind direction differed only by one angular bin class (15º), we considered both directions as being the same.

In Table 6, where we compare the wind directions inferred from dust devil tracks with the predicted wind directions for Aeolis quadrangle, only 20% of the values agree for the three altitude values. The results obtained for the other 4 quadrangles

Table 9
Comparison between calculated prevailing wind direction and predicted wind direction for Hellas.

ID	L_s[deg.]	Local Time	Calculated [deg.]	CPBL [m]	Predicted [deg.]		
					50 m	1000 m	CPBL
E10-00012_C1	263.49	14:17	165-345	5400	120-300	120-300	120-300
E10-00578_C	266.02	14:18	150-330	6700	15-195	0-180	0-180
S09-01218_C	267.20	14:17	135-315	7300	165-345	0-180	0-180
E10-02468_C3	273.23	13:58	90-270	4800	60-240	60-240	60-240
E10-02820_C	274.51	13:56	60-240	4900	60-240	60-240	60-240
E11-01296_C	286.63	13:53	165-345	6300	150-330	150-330	150-330
E11-00727_C1	284.72	13:57	45-225	5800	150-330	150-330	165-345
E11-00727_C2	284.72	13:57	0-180	5800	150-330	150-330	165-345
E11-00727_C3	284.72	13:57	150-330	5800	150-330	150-330	165-345
E10-04932_C	282.14	13:57	105-285	6200	105-285	105-285	165-345
E10-01933_C	271.23	14:07	0-180	6600	120-300	120-300	150-330
E11-00173_C	282.75	14:00	60-240	7200	165-345	165-345	165-345
E10-02444_C	273.12	14:02	150-330	6600	45-225	45-225	15-195
E11-01270_C	286.53	13:51	45-225	7000	0-180	0-180	15-195
E12-01277_C1	307.63	13:27	75-255	4800	60-240	60-240	45-225
E12-01277_C2	307.63	13:27	75-255	4800	60-240	60-240	45-225
E12-01277_C3	307.63	13:27	105-285	4800	60-240	60-240	45-225
E12-01752_C	310.02	13:36	30-210	5200	150-330	150-330	150-330
E12-00190_C1	302.08	13:30	30-210	5800	165-345	165-345	120-300
E12-00190_C2	302.08	13:30	120-300	5800	165-345	165-345	120-300
E1301622_C	329.28	13:23	75-255	4200	60-240	60-240	60-240
E13-00975_C	325.28	13:23	60-240	4300	60-240	60-240	60-240
R12-01589_C	316.21	13:50	105-185	5100	150-330	150-330	150-330
R1201264_C	314.38	13:49	15-195	6300	150-330	150-330	165-345
ESP_014399_1220_C	325.60	14:34	75-255	5700	120-300	120-300	120-300
ESP_014176_1155_C1	315.80	14:34	165-345	5100	150-330	150-330	150-330
ESP_014176_1155_C2	315.80	14:34	15-195	5100	150-330	150-330	150-330
ESP_014176_1155_C3	315.80	14:34	45-225	5100	150-330	150-330	150-330
ESP_014176_1155_C4	315.80	14:34	150-330	5100	150-330	150-330	150-330
ESP_014176_1155_C5	315.80	14:34	150-330	5100	150-330	150-330	150-330
ESP_014176_1155_C6	315.80	14:34	0-180	5100	150-330	150-330	150-330
ESP_014108_1200_C1	312.70	14:37	30-210	6800	150-330	150-330	150-330
ESP_014108_1200_C2	312.70	14:37	120-300	5100	150-330	150-330	150-330
ESP_014070_1170_C	311.00	14:43	90-270	5500	120-300	120-300	135-315
ESP_014069_1180_C	311.00	14:39	30-210	6700	135-315	135-315	150-330
ESP_014056_1180_C	310.40	14:40	75-255	6800	120-300	120-300	150-330
ESP_014004_1180_C	308.00	14:41	120-300	5600	120-300	120-300	150-330
ESP_013991_1160_C	307.40	14:43	120-300	5500	135-315	135-315	150-330
ESP_013965_1165_C	306.20	14:43	150-330	5600	135-315	135-315	150-330
PSP_006264_1420_C	359.90	14:28	45-235	4000	45-225	45-225	45-225

are similar, not showing a high percentage of concordance between calculated and predicted wind directions. For Argyre (Table 7), we have found that ~39% of the predictions at 50 m and at 1000 m, and ~20% of the predictions at the CPBL height agreed with the measurements. For Noachis (Table 8), we have found that ~33% of the predictions at 50 m and at 1000 m, and ~31% of the predictions at the CPBL height agreed with the measurements. For Hellas (Table 9), we have found that ~35% of the predictions at 50 m and at 1000 m, and ~25% of the predictions at the CPBL height agreed with the measurements. Finaly, we have found, for Eridania (Table 10), that ~18% of the predictions at 50 m, ~22% at 1000 m, and ~27% of the predictions at the CPBL height agreed with the measurements. The diverging results for Argyre, when compared to those from Statella et al. (2014), are due to the coarser precision of the measured directions. In Statella et al. (2014) angular steps of 45° were adopted, instead of 15° used here. As the measurement details in the latter were coarser, the prevailing wind direction from the MCD in that case was considered to be the one showing a higher wind speed between N-S and EW components.

When we considered the whole set of 200 images, only 32%, 33% and 25% of the extractions at 50 m, 1000 m and at the CPBL height, respectively, agreed with the dust devil tracks prevailing direction measurements. Table 11 summarizes the results for each quadrangle and also for the whole set of images.

In addition, we have extracted the surface wind stress using the MCD for the whole set of images. According to Haberle et al. (2003), a threshold stress of 0.0225 Nm^{-2} would be needed to lift dust through bombardment from sand saltation. This has also been found to be true by Kahre et al. (2006), which used the NASA Ames general circulation model to investigate the mechanisms responsible for the observed martian dust cycle. According to their results, dust devil and wind stress lifting should both contribute to the simulated amount of dust found on the atmosphere. In our results, in none of the cases the large scale wind surface stress was higher than that threshold. The highest value we have found was ~ 0.0108 Nm^{-2}, extracted from the MCD using the local time 16:00h, φ~54°S, λ~13°E and L_s~182°. In such cases, the suction effect caused by the dust devils low-pressure cores must have assisted the wind stress in order to lift particles, as it has already been stated by Greeley et al. (1981), Greeley and Iversen (1985) and Greeley et al. (2003).

5. Conclusions

We have applied an automated method based on directional morphological openings to infer the prevailing dust devil tracks direction to a dataset of 200 images from Aeolis, Argyre, Eridania, Noachis and Hellas quadrangles. Next, we have compared the

Table 10
Comparison between calculated prevailing wind direction and predicted wind direction for Eridania.

ID	L_s[deg.]	Local Time	Calculated [deg.]	CPBL [m]	Predicted [deg.]		
					50 m	1000 m	CPBL
E10-00563	265.98	14:06	105-285	7200	120-300	120-300	105-285
E09-02016	259.51	14:16	165-345	6600	105-285	105-285	60-240
R09-03051	266.28	14:23	150-330	6700	15-195	15-195	15-195
R09-01707	261.74	14:28	150-330	6600	30-210	30-210	30-210
ESP_021874_1175_P1	262.80	15:13	135-315	5700	15-195	0-180	150-330
ESP_021874_1175_P2	262.80	15:13	120-300	5700	15-195	0-180	150-330
ESP_021874_1175_P3	262.80	15:13	105-285	5700	15-195	0-180	150-330
ESP_021939_1170	266.00	15:10	75-255	6200	105-285	120-300	150-330
ESP_021940_1205_P1	266.00	15:07	45-225	5900	0-180	165-345	165-345
ESP_021940_1205_P2	266.00	15:07	120-300	5900	0-180	165-345	165-345
ESP_021940_1205_P3	266.00	15:07	120-300	5900	0-180	165-345	165-345
PSP_004086_1180_P1	255.10	15:25	165-345	5200	30-210	30-210	165-345
PSP_004086_1180_P2	255.10	15:25	60-240	5200	30-210	30-210	165-345
PSP_004086_1180_P3	255.10	15:25	45-225	5200	30-210	30-210	165-345
E10-04027	278.89	14:02	15-195	7000	0-180	0-180	0-180
E11-01652	287.74	13:46	30-210	6500	165-345	0-180	30-210
E11-01664	287.79	13:53	0-180	7200	0-180	0-180	0-180
E11-02785	292.18	13:46	165-345	6800	0-180	0-180	0-180
E11-02787	292.18	13:45	0-180	6500	0-180	0-180	0-180
E11-02045	289.04	13:40	0-180	6000	165-345	165-345	120-300
R09-04267_P1	270.71	14:16	60-240	6300	105-285	105-285	45-225
R09-04267_P2	270.71	14:16	150-330	6300	105-285	105-285	45-225
R10-04120	285.52	14:07	135-315	7700	0-180	0-180	0-180
R11-02327	298.55	13:50	45-225	6000	30-210	30-210	0-180
R10-03758	284.16	14:10	135-315	6800	165-345	165-345	0-180
R10-02441	279.70	14:15	165-345	6800	165-345	165-345	165-345
R10-03959_P1	284.82	14:10	120-300	6600	165-345	165-345	0-180
R10-03959_P2	284.82	14:10	120-300	6600	165-345	165-345	0-180
R10-04815	287.98	14:06	15-195	6700	165-345	165-345	0-180
R10-03563_P1	283.55	14:12	45-225	6400	165-345	165-345	0-180
R10-03563_P2	283.55	14:12	135-315	6400	165-345	165-345	0-180
R11-02811	299.83	13:51	0-180	6800	135-315	135-315	0-180
E11-04510	300.81	13:36	165-345	6100	120	135-315	0-180
R12-00250	309.59	13:43	30-210	6200	105-285	120-300	0-180
R12-02283	319.06	13:40	15-195	5800	90-270	105-285	165-345
PSP_005510_1290	322.40	14:25	0-180	6200	60-240	75-255	120-300
ESP_023021_1160_P1	317.10	14:30	90-270	5300	120-300	135-315	150-330
ESP_023021_1160_P2	317.10	14:30	75-255	5300	120-300	135-315	150-330
ESP_023021_1160_P3	317.10	14:30	90-270	5300	120-300	135-315	150-330
ESP_023021_1160_P4	317.10	14:30	105-285	5300	120-300	135-315	150-330
ESP_023021_1160_P5	317.10	14:30	105-285	5300	120-300	135-315	150-330
ESP_023021_1160_P6	317.10	14:30	75-255	5300	120-300	135-315	150-330
ESP_014121_1180	313.30	14:38	150-330	6600	165-345	165-345	150-330
R13-01492	331.07	13:48	15-195	5100	45-225	45-225	120-300
PSP_006248_1235	353.20	14:34	0-180	5100	105-285	105-285	105-285

Table 11
Summary of the results for the comparison between measured and predicted wind directions for each of the quadrangles and for the whole set of images.

	Number of images	Altitude		
		50 m	1000 m	CPBL
Aeolis	5	20%	20%	20%
Argyre	71	39%	39%	20%
Noachis	39	33%	33%	31%
Hellas	40	35%	35%	25%
Eridania	45	18%	22%	27%
For the whole dataset	200	32%	33%	25%

inferred directions with the MCD predicted wind directions for different altitudes from the surface: 50 m, 1000 m and at the CPBL height. In all cases the accordance between measurements and predictions is low. In the best case (for 1000 m above the surface), this value reaches 33%, considering a tolerance of 15° (the angular steps adopted when measuring dust devil tracks directions). All the results are very similar, with the prediction performed using the CPBL height giving the worst agreement with the dust devil tracks prevailing direction measurements. Taken individually, none of the quadrangles showed a conformity between measured and predicted directions higher than 39%. This seems to be a good indicator that the MCD fails to predict local wind patterns, such as the ones driving dust devil vortices on the surface of Mars, perhaps due to an insufficient resolution. Therefore, for a more local scale, the dominant wind direction should be inferred preferably by methods other than the MCD simulations, namely from the analysis of the dust devil tracks prevailing orientations. For that purpose, we intend to perform a systematic collection of image data showing dust devil tracks, specifically from several representative sites in several time periods, aided by recent platforms that facilitate checking about the availability of multi-temporal imagery of high resolution in order to quantify the changes of these dynamic surface processes on Mars (Sidiropoulos and Muller, 2015; Erkeling et al., 2016).

In addition, the extractions for the surface wind stress at each scene center coordinates was never higher than the threshold stress of 0.0225 Nm^{-2} needed to lift dust even though there are dust devil tracks. It agrees with results from Greeley et al. (1981), Greeley and Iversen (1985) and Kahre et al. (2006) and reinforces

that dust devil vortices, as well as other mechanisms such as slope winds (Rafkin et al., 2002) and rocket dust storms (Spiga et al., 2013), are important actors in lifting dust particles, contributing to the local atmosphere opacity and surface modification.

References

Balme, M.R., Greeley, R., 2006. Dust devils on Earth and Mars. ReviewsofGeophysics 44, RG3003.

Balme, M.R., Whelley, P.L., Greeley, R., 2003. Mars: dust devil track survey in Argyre Planitia and Hellas Basin. J. Geophys. Res. 108 (E8).

Erkeling, G., Luesebrink, D., Hiesinger, H., Reiss, D., Heyer, T., Jaumann, R., 2016. The Multi-Temporal Database of Planetary Image Data (MUTED): A database to support the identification of surface changes and short-lived surface processes. Planet. SpaceSci. http://dx.doi.org/10.1016/j.pss.2016.03.002

Fenton, L.K., Lorenz, R., 2015. Dust devil height and spacing with relation to the martian planetary layer thickness. Icarus 260, 246–262.

Forget, F., Hourdin, F., Fournier, R., Hourdin, C., Talagrand, O., Collins, M., Lewis, S.R., Read, P.L., Huot, J.-P., 1999. Improved general circulation models of the martian atmosphere from the surface to above 80 km. J. Geophys. Res. 104 (E10), 24155–24175.

Greeley, R., Iversen, J., 1985. Wind as a Geologic Process on Earth, Mars, Venus and Titan. Cambridge Univ. Press, New York.

Greeley, R., White, B., Pollack, J.B., Iversen, J., Leach, R.N., 1981. Dust storms on Mars: Considerations and simulations, in Desert Dust: Origin, Characteristics, and Effect on Man edited by T. Péwé. Spec. Pap. Geol. Soc. Am 186, 101–121.

Greeley, R., et al., 2003. Martian dust devils: Laboratory simulations of particle threshold. J. Geophys. Res. 108, E5.

Haberle, R., Houben, H., Hertenstein, R., Herdtle, T., 1993. A boundary layer model for Mars: Comparison with Viking lander and entry data. J. Atmos. Sci. 50, 1544–1559.

Haberle, M.H., Murphy, J.R., Schaeffer, J., 2003. Orbital change experiments with a Mars general circulation model. Icarus 161, 66–89.

Hinson, D.P., Pätzold, M., Tellmann, S., Häusler, B., Tyler, G.L., 2008. The depth of the convective boundary layer on Mars. Icarus 198, 57–66.

Kahre, M.A., Murphy, J.R., Haberle, R.M., 2006. Modeling the Martian dust cycle and surface dust reservoirs with the NASA Ames general circulation model. J. Geophys. Res. Planets 111, 10.1029/2005je002588.

Lewis, S.R., Collins, M., Read, P.L., Forget, F., Hourdin, F., Fournier, R., Hourdin, C., Talagrand, O., Huot, J.P., 1999. A climate database for Mars. J. Geophys. Res. Planets 104, E10.

Malin, M.C., Edgett, K.S., 2001. Mars Global Surveyor Mars Orbiter Camera: interplanetary cruise through primary mission. J. Geophys. Res. 106, E10.

Petrosyan, A., Galperin, B., Larsen, S.E., Lewis, S.R., Määttänen, A., Read, P.L., Renno, N., Rogberg, L.P.H.T., Savijärvi, H., Siili, T., Spiga, A., Toigo, A., Vázquez, L., 2011. The Martian armospheric boundary layer. ReviewsofGeophysics 49, RG3005. http://dx.doi.org/10.1029/2010RG000351.

Rafkin, S.C.R., Maria, M.R.V.S., Michaels, T.I., 2002. Simulation of the atmospheric thermal circulation of a martian volcano using a mesoscale numerical model. Nature 419, 697–699.

Rennó, N.O., Burkett, M.L., Larkin, M.P., 1998. A simple thermodynamical theory for dust devils. J. Atmos. Sci. 55, 3244–3252.

Sidiropoulos, P., Muller, J.-P., 2015. On the status of orbital high-resolution repeat imaging of Mars for the observation of dynamic surface processes. Planet. SpaceSci. 117, 207–222.

Soille, P., 2004. Morphological Image Analysis. Springer-Verlag, Berlin.

Spiga, A., Faure, J., Madeleine, J.B., Maatanen, A., Forget, F., 2013. Rocket dust storms and detached dust layers in the martian atmosphere. J. Geophys. Res. ((Planets)) 118, 746–767.

Statella, T., Pina, P., Silva, E.A., 2012. Image processing algorithm for the identification of Martian dust devil tracks in MOC and HiRISE images. Planet. Space. Sci. 70, 46–58.

Statella, T., Pina, P., Silva, E.A., 2014. Automated determination of the orientation of dust devil tracks in Mars orbiter images. Adv. SpaceRes. 53, 1822–1833.

Statella, T., 2015. Mapping Mars: Geodetic and cartographic aspects. Planet. SpaceSci. 108, 1–12.

Statella, T., Pina, P., Silva, E.A., 2015. Extensive computation of albedo contrast between Martian dust devil tracks and their neighboring regions. Icarus 250, 43–52.

Statella, T., Pina, P., Silva, E.A., 2016. Automated width measurements of Martian dust devil tracks. AeolianResearch 20, 1–6.

Thomas, P.C., Gierasch, P., Sullivan, R., Miller, D.S., Cartillo, E.A., Cantor, B., Mellon, M.T., 2003. Mesoscale linear streaks on Mars: environments of dust entrainment. Icarus 162, 242–258.

Whelley, P., Greeley, R., 2006. Latitudinal dependency in dust devil activity on Mars. J. Geophys. Res. 111, E10003.